CM² MAGAZINE

第 68 期

南方科技大学海洋磁学中心主编

https://cm².sustech.edu.cn/

创刊词

海洋是生命的摇篮，是文明的纽带。地球上最早的生命诞生于海洋，海洋里的生命最终进化成了人类，人类的文化融合又通过海洋得以实现。人因海而兴。

人类对海洋的探索从未停止。从远古时代美丽的神话传说，到麦哲伦的全球航行，再到现代对大洋的科学钻探计划，海洋逐渐从人类敬畏崇拜幻想的精神寄托演变成可以开发利用与科学研究的客观存在。其中，上个世纪与太空探索同步发展的大洋科学钻探计划将人类对海洋的认知推向了崭新的纬度：深海（deep sea）与深时（deep time）。大洋钻探计划让人类知道，奔流不息的大海之下，埋藏的却是亿万年的地球历史。它们记录了地球板块的运动，从而使板块构造学说得到证实；它们记录了地球环境的演变，从而让古海洋学方兴未艾。

在探索海洋的悠久历史中，从大航海时代的导航，到大洋钻探计划中不可或缺的磁性地层学，磁学发挥了不可替代的作用。这不是偶然，因为从微观到宏观，磁性是最基本的物理属性之一，可以说，万物皆有磁性。基于课题组的学科背景和对海洋的理解，我们对海洋的探索以磁学为主要手段，海洋磁学中心因此而生。

海洋磁学中心，简称 CM^2，一为其全名“Centre for Marine Magnetism”的缩写，另者恰与爱因斯坦著名的质能方程 $E = MC^2$ 对称，借以表达我们对科学巨匠的敬仰和对科学的不懈追求。

然而科学从来不是单打独斗的产物。我们以磁学为研究海洋的主攻利器，但绝不仅限于磁学。凡与磁学相关的领域均是我们关注的重点。为了跟踪反映国内外地球科学特别是与磁学有关的地球科学领域的最新研究进展，海洋磁学中心特地主办 CM^2 Magazine，以期与各位地球科学工作者相互交流学习、合作共进！

“海洋孕育了生命，联通了世界，促进了发展”。 21 世纪是海洋科学的时代，由陆向海，让我们携手迈进中国海洋科学的黄金时代。

目 录

1. 中国中部地区在 40 Ma 出现黄土质粉尘

翻译人：仲义 zhongy@sustech.edu.cn

Niels M, Guillaume D N, Natasha B, et al. ***Loess-Like dust appearance at 40 Ma in Central China [J]*** *Paleoceanography and Paleoclimatology 2021, 563, 116882.*

https://doi.org/10.1016/j.epsl.2021.116882

摘要：亚洲粉尘在区域性到全球尺度上气候和沉积方面的作用得到广泛研究，这使亚洲过去的大气环流得以重建。然而，粉尘沉积的时间和来源仍然存在争议，从中新世到始新世时期，亚洲大陆有大量的黄土记录，这些记录与各种机制有关，包括全球变冷、青藏高原隆升和内陆特提斯海的撤退。本文以中国中部西宁盆地始新世陆相泥岩为研究对象，利用粒度分布的端元分析方法，识别了 40 Ma 记录中出现的黄土质粉尘组分。这与高纬度轨道周期的开始是一致的，并且在相同的记录中显示了草原-沙漠植被的转变。进而，作者从风成沙丘沉积物得出的当时以类似于现今冬季季风的西北风，受控于西伯利亚上空的高压系统。作者认为 40 Ma 的观测变化反映了西伯利亚高压与西风水汽在斜率周期上的相互作用，并促进了中国中部的沙尘暴和干旱化。从时间上看，这次爆发可能是由于古特提斯洋的撤退导致的大陆增生所引发的。

ABSTRACT: Asian mineral dust has been studied extensively for its role in affecting regional-to globalscale climate and for its deposits, which enable reconstructing Asian atmospheric circulation in the past. However, the timing and origin of the dust deposits remain debated. Numerous loess records have been reported across the Asian continent with ages varying from the Miocene to the Eocene and linked to various mechanisms including global cooling, Tibetan Plateau uplift and retreat of the inland protoParatethys Sea. Here, we study the Eocene terrestrial mudrocks of the Xining Basin in central China and use nonparametric end-member analysis of grain-size distributions to identify a loess-like dust component appearing in the record at 40 Ma. This is coeval with the onset of high-latitude orbital cycles and a shift to predominant steppe-desert vegetation as recognized by previous studies in the same record. Furthermore, we

derive wind directions from eolian dune deposits which suggest northwesterly winds, similar to the modern-day winter monsoon which is driven by a high-pressure system developing over Siberia. We propose that the observed shifts at 40 Ma reflect the onset of the Siberian High interacting with westerly derived moisture at obliquity timescales and promoting dust storms and aridification in central China. The timing suggests that the onset may have been triggered by increased continentality due to the retreating proto-Paratethys Sea.

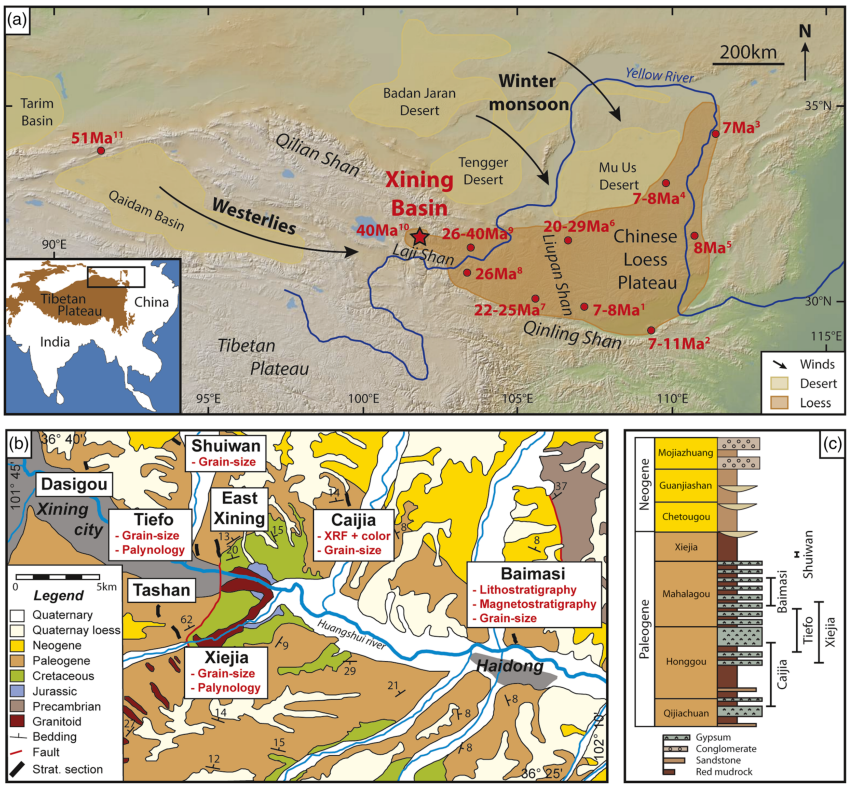

Fig1. Modern-day topographic map (http://www.geomapapp.org) of the northeastern Tibetan Plateau showing various reported ages for the onset of loess-like deposits (modified from Meijer et al., 2020): (1) central Loess Plateau: Z. L. Ding et al. (2001); Y. Song et al. (2001); D. Sun et al. (1997); D. Sun, Shaw, et al. (1998); D. Sun, An, et al. (1998); (2) southern Loess Plateau: Zheng et al. (1992); D. Sun et al. (1997); Wang et al. (2014); (3) Baode: Y. Zhu et al. (2008); (4) Jiaxian: Ding et al. (1998); Qiang et al. (2001); (5) Shilou: Xu et al. (2009); age reinterpreted by Ao et al. (2016); (6) Sikouzi: Jiang et al. (2010); age reinterpreted by W. T. Wang et al. (2011); (7) Tianshui Basin: Guo et al. (2002); record extended by X. Qiang et al. (2011); (8) Linxia Basin: Garzione et al. (2005); (9) Lanzhou Basin: Y. Zhang et al. (2014); age reinterpreted by W. Wang et al. (2016);

(10) Xining Basin: Licht et al. (2014); (11) Xorkol Basin (Li et al., 2018). The Xining Basin is indicated with a star. (b) Geological map of the Xining Basin based on BGMRQP (1965), QBGMR (1985), and Dai et al. (2006) showing the locations of the sections in the Xining Basin. Datasets generated in this study are indicated in red. (c) Lithostratigraphy listing the formations of the Xining Basin adapted from Horton et al. (2004) and updated following Fang et al. (2019). Stratigraphic intervals covered by the datasets of this study are indicated on the right.

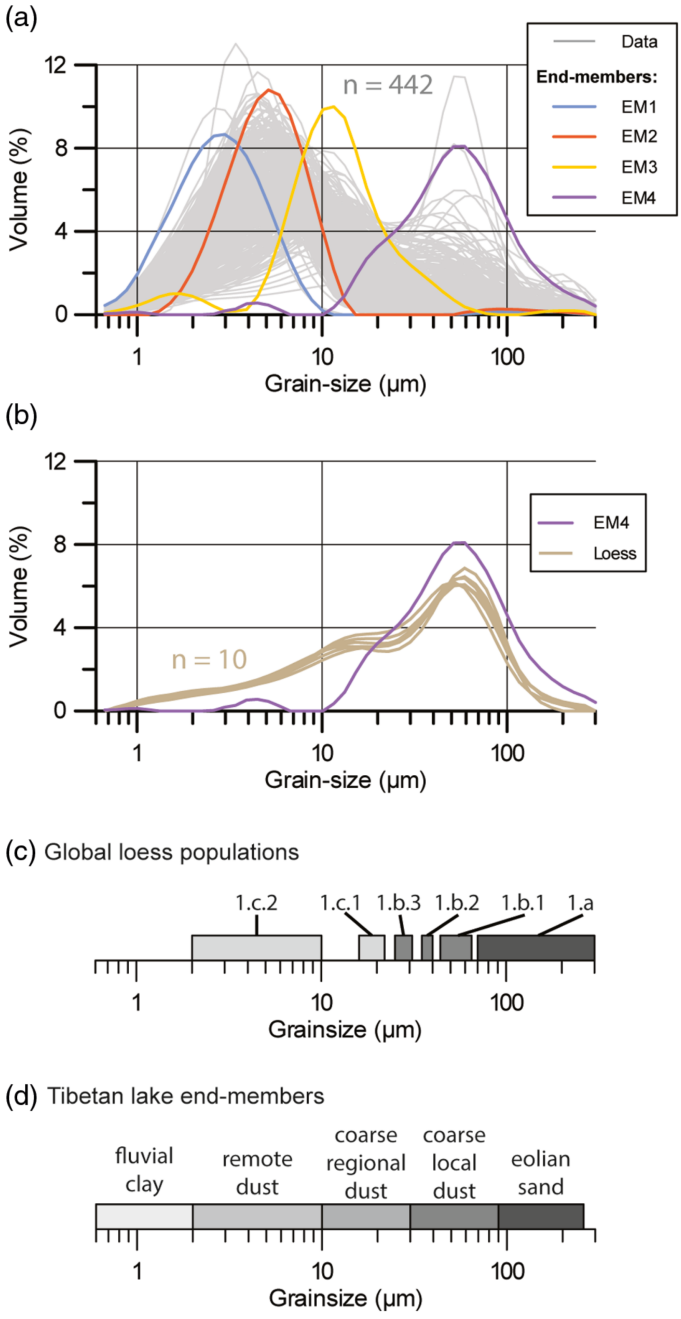

Fig2. (a) Frequency curves of the total measured GSDs and of the end-members. (b) Comparison of EM4 with the GSD of local Quaternary loess in the Xining Basin. (c) Size ranges of global loess populations identified by Vandenberge (2013). (d) Size ranges of end-members in Tibetan lake records (Dietze et al., 2014). GSD, grain-size distribution.

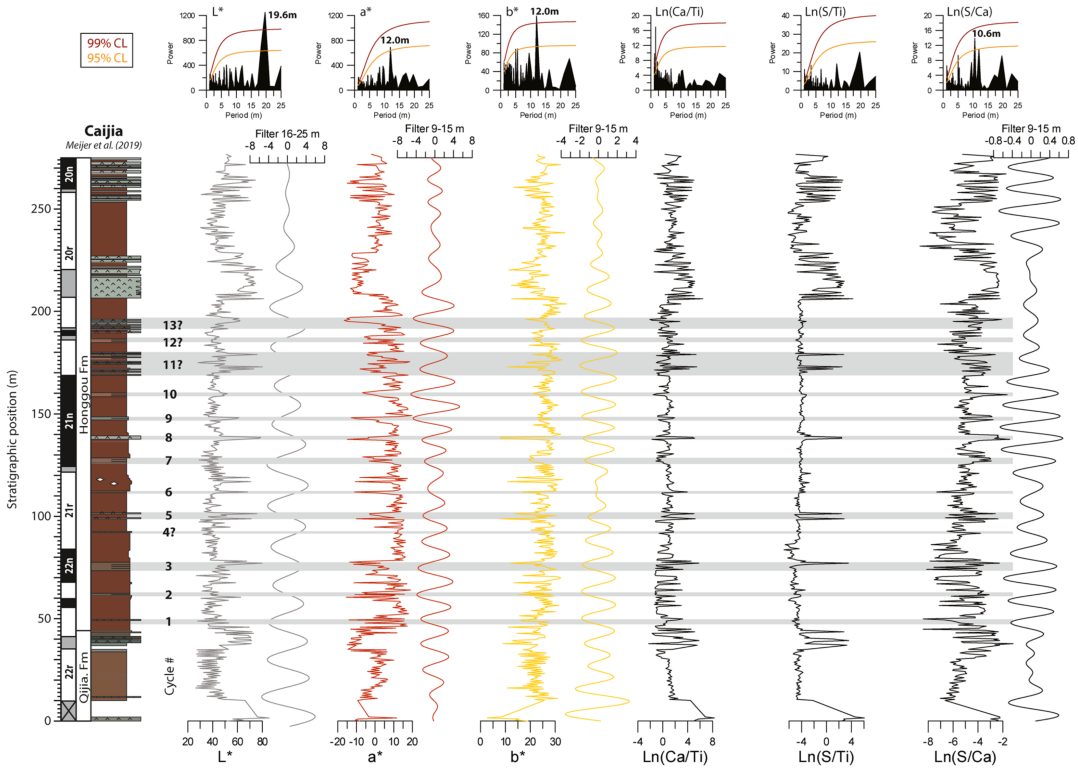

Fig3. Time series of the Caijia section showing the color records: L* (lightness), a* (red over green) and b* (yellow over blue) and XRF record of log-ratios: Ca/Ti, S/Ti and Ca/S. Redfit spectral analyses with confidence limits (CL) are shown above and the bandpass filters using the dominant period of the individual records are shown on the right. The cycles are numbered and the wet phases represented by lacustrine mudrocks, gypsum beds and fluvial sandstones are marked in gray. Litho- and magnetostratigraphy is from Meijer et al. (2019). XRF, X-Ray Fluorescence.

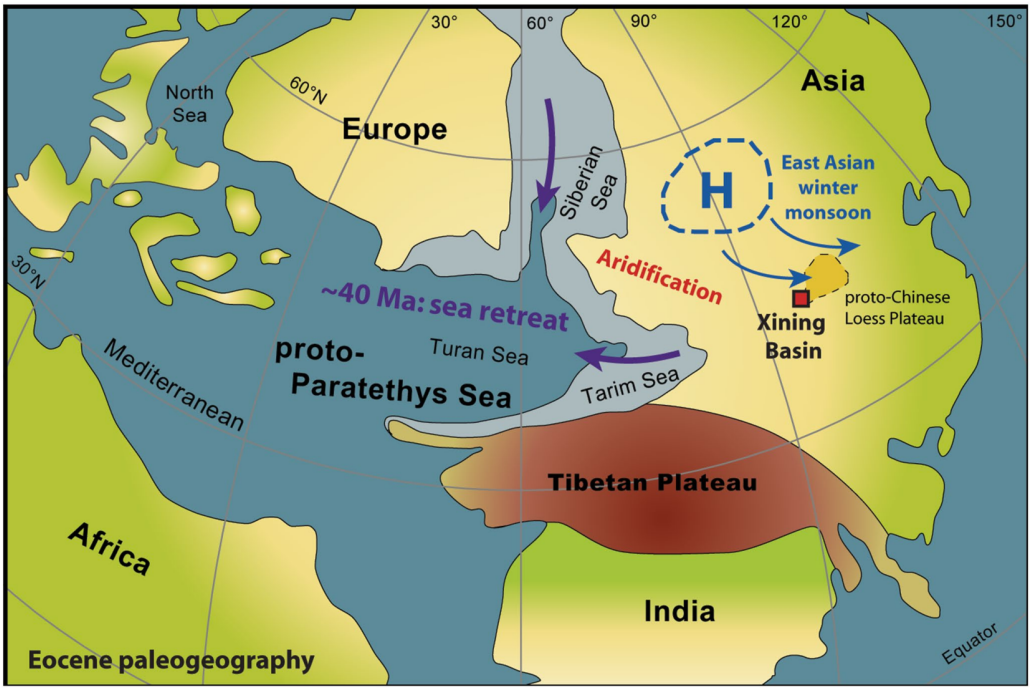

Fig4. Eocene paleogeography of Eurasia (modified from Bosboom et al., 2011) showing the retreat of the proto-Paratethys Sea. This may have resulted in aridification and the onset of a high-pressure system over Siberia driving the East Asian winter monsoon and dust storms in the Xining Basin.

2. 萨摩亚单斜辉石的同位素高度不均一性限定沉积物的再循环

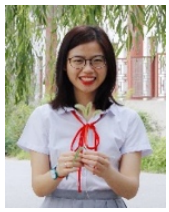

翻译人：冯婉仪 fengwy@sustech.edu.cn

Adams J V, Jackson M G, Spera F J, et al. ***Extreme isotopic heterogeneity in Samoan clinopyroxenes constrains sediment recycling[J]****. Nature Communications, 2021, 12:1234. https://doi.org/10.1038/s41467-021-21416-9*

摘要：热点火山喷发的熔岩提供了地幔不均一性的证据。高 $^{87}Sr/^{86}Sr$（> 0.706）的萨摩亚岛熔岩代表了一个包含古老俯冲沉积物的地幔源区。为了进一步揭示这一源区的性质，我们以萨摩亚萨瓦伊岛的一个高 $^{87}Sr/^{86}Sr$ 熔岩为研究对象，详细分析了熔岩中单斜辉石的 $^{87}Sr/^{86}Sr$、$^{143}Nd/^{144}Nd$ 同位素组成和主、微量元素含量。我们发现单斜辉石表现出显著的 $^{87}Sr/^{86}Sr$ 同位素变化范围，约占大洋地幔总不均一性的 30%，其中包括了在大洋热点熔岩中观测到的最高 $^{87}Sr/^{86}Sr$ 值。这些新的同位素数据、来自其他萨摩亚熔岩的数据以及岩浆混合计算结果显示单斜辉石 $^{87}Sr/^{86}Sr$ 同位素的变化是高硅、高 $^{87}Sr/^{86}Sr$（高达 0.7316）岩浆和低硅、低 $^{87}Sr/^{86}Sr$ 岩浆混合导致的。这些结果为深入了解来自沉积物交代地幔源区的岩浆组成的提供了机会，并记录了沉积物循环至地幔的命运。

ABSTRACT: Lavas erupted at hotspot volcanoes provide evidence of mantle heterogeneity. Samoan Island lavas with high $^{87}Sr/^{86}Sr$ (> 0.706) typify a mantle source incorporating ancient subducted sediments. To further characterize this source, we target a single high $^{87}Sr/^{86}Sr$ lava from Savai'i Island, Samoa for detailed analyses of $^{87}Sr/^{86}Sr$ and $^{143}Nd/^{144}Nd$ isotopes and major and trace elements on individual magmatic clinopyroxenes. We show the clinopyroxenes exhibit a remarkable range of $^{87}Sr/^{86}Sr$—including the highest observed in an oceanic hotspot lava—encompassing ~ 30% of the oceanic mantle's total variability. These new isotopic data, data from other Samoan lavas, and magma mixing calculations are consistent with clinopyroxene $^{87}Sr/^{86}Sr$ variability resulting from magma mixing between a high silica, high $^{87}Sr/^{86}Sr$ (up to 0.7316) magma, and a low silica, low $^{87}Sr/^{86}Sr$ magma. Results provide insight

into the composition of magmas derived from a sediment-infiltrated mantle source and document the fate of sediment recycled into Earth's mantle.

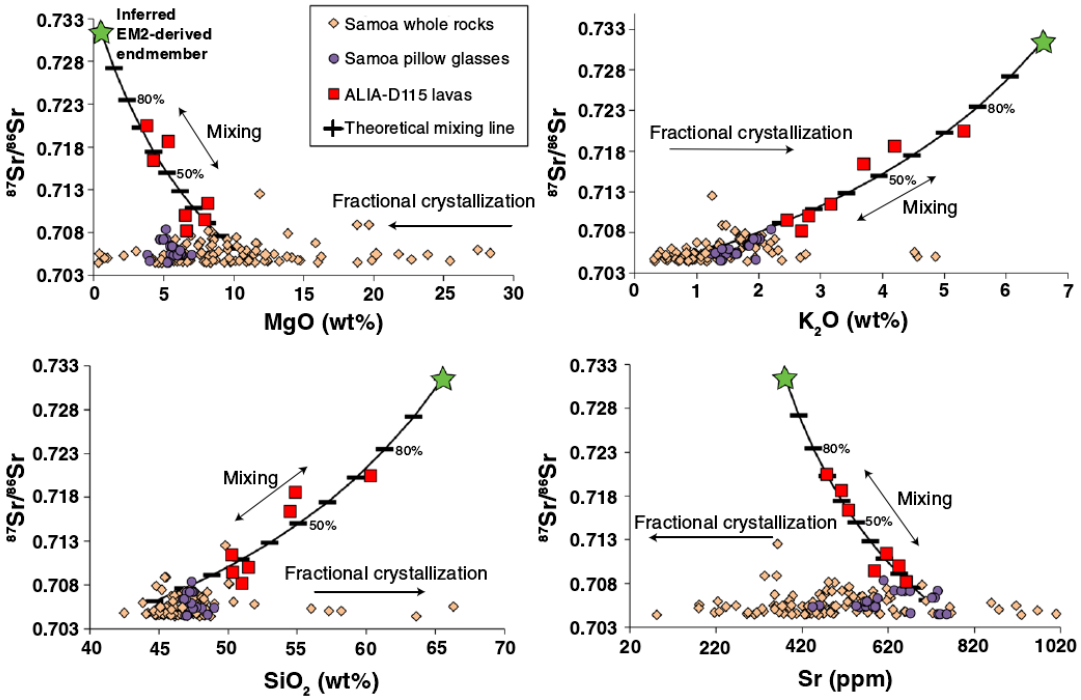

Fig1. $^{87}Sr/^{86}Sr$ versus element concentration showing theoretical mixing curves of inferred end-member compositions. The direction of fractional crystallization is denoted by arrows. The green star denotes the EM2-derived mixing end-member composition (SiO_2 = 65.5 wt%, MgO = 0.5 wt%, Al_2O_3 = 17.1 wt%, FeO = 3.8 wt%, CaO = 2.7 wt%, TiO_2 = 1 wt%, and $Na_2O + K_2O$ = 11 wt%; see Supplementary Table 2), which is calculated in this study (see "Methods"); the black hatched line shows the path of the calculated mixing curves, where each hatch increases by 10% mixing from the geochemically depleted mafic end-member to the more evolved EM2-derived end-member (black hatched line is derived from the same methodology as described briefly in Fig. 2 and in the "Methods"). Mixing is clearly defined by a curve with a non-zero slope, and is unlike the lavas that have been affected only by fractional crystallization (which have zero-slope trends). The ALIA-D115 lavas are represented by red squares, the other Samoan whole rock lavas by orange diamonds, and Samoan pillow glasses by purple circles. See Fig. 1 caption for data references; Samoa pillow glass data can be found in Workman et al.[6]. All errors bars smaller than symbols.

3. 海洋碳酸钙溶解模式

翻译人:李园洁 liyj3@sustech.edu.cn

Sulpis O, Jeansson E, Dinauer A, et al. ***Calcium carbonate dissolution patterns in the ocean[J].*** *Nature Geoscience, 2021.*

https://doi.org/10.1038/s41561-021-00743-y

摘要：海洋生物分泌的碳酸钙在大洋中非常普遍。这些颗粒沉降，大部分溶解到更深的水或海底。碳酸盐的溶解稀释了大洋，但是溶解的垂向和区域分布和幅值还不清楚。本文利用海水化学和年龄数据获得主要大洋区域的远洋碳酸钙溶解速率，提供了数据为基础的区域碳酸钙沉降通量剖面。我们发现在 300m 深全球碳酸钙输出 76 ± 12 Tmol yr^{-1}，其中 36 ± 8 Tmol (47%) 溶解在水体中。溶解发生在两个不同的深度层。在浅水，新陈代谢 CO_2 释放, 高镁方解石主导溶解而深水碳酸钙溶解性增加主导溶解。基于重建的沉降通量，我们的数据表明高生产力上涌地区比贫营养系统具有更高的从海面到海底碳酸钙转换效率。这个结果对评估未来大洋酸化和古记录的解释具有重要意义，因为他们证明了不仅内部海洋化学，还有海平面生态系统对控制碳酸钙颗粒的溶解具有重要影响。

ABSTRACT: Calcium carbonate ($CaCO_3$) minerals secreted by marine organisms are abundant in the ocean. These particles settle and the majority dissolves in deeper waters or at the seafloor. Dissolution of carbonates buffers the ocean, but the vertical and regional distribution and magnitude of dissolution are unclear. Here we use seawater chemistry and age data to derive pelagic $CaCO_3$ dissolution rates in major oceanic regions and provide the first data-based, regional profiles of CaCO3 settling fluxes. We find that global $CaCO_3$ export at 300 m depth is 76 ± 12 Tmol yr^{-1}, of which 36 ± 8 Tmol (47%) dissolves in the water column. Dissolution occurs in two distinct depth zones. In shallow waters, metabolic CO_2 release and high-magnesium calcites dominate dissolution while increased $CaCO_3$ solubility governs dissolution in deeper waters. Based on reconstructed sinking fluxes, our data indicate a higher $CaCO_3$ transfer

efficiency from the surface to the seafloor in high-productivity, upwelling areas than in oligotrophic systems. These results have implications for assessments of future ocean acidification as well as palaeorecord interpretations, as they demonstrate that surface ecosystems, not only interior ocean chemistry, are key to controlling the dissolution of settling $CaCO_3$ particles.

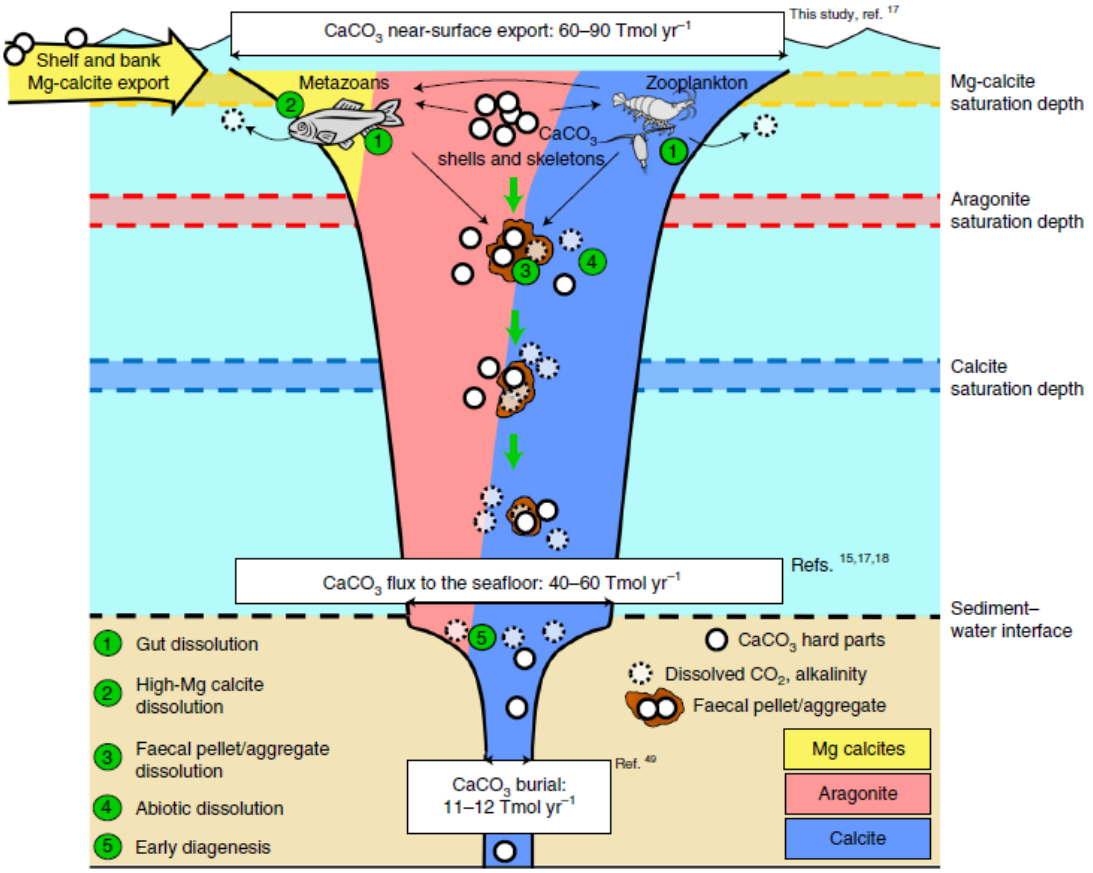

Fig 1. Conceptual view of the oceanic $CaCO_3$ cycle. Fluxes given in Tmol yr^{-1} are the $CaCO_3$ export flux from the surface ocean, the $CaCO_3$ flux reaching the seafloor and the $CaCO_3$ flux buried in sediments. Green circles indicate the five main mechanisms of dissolution.

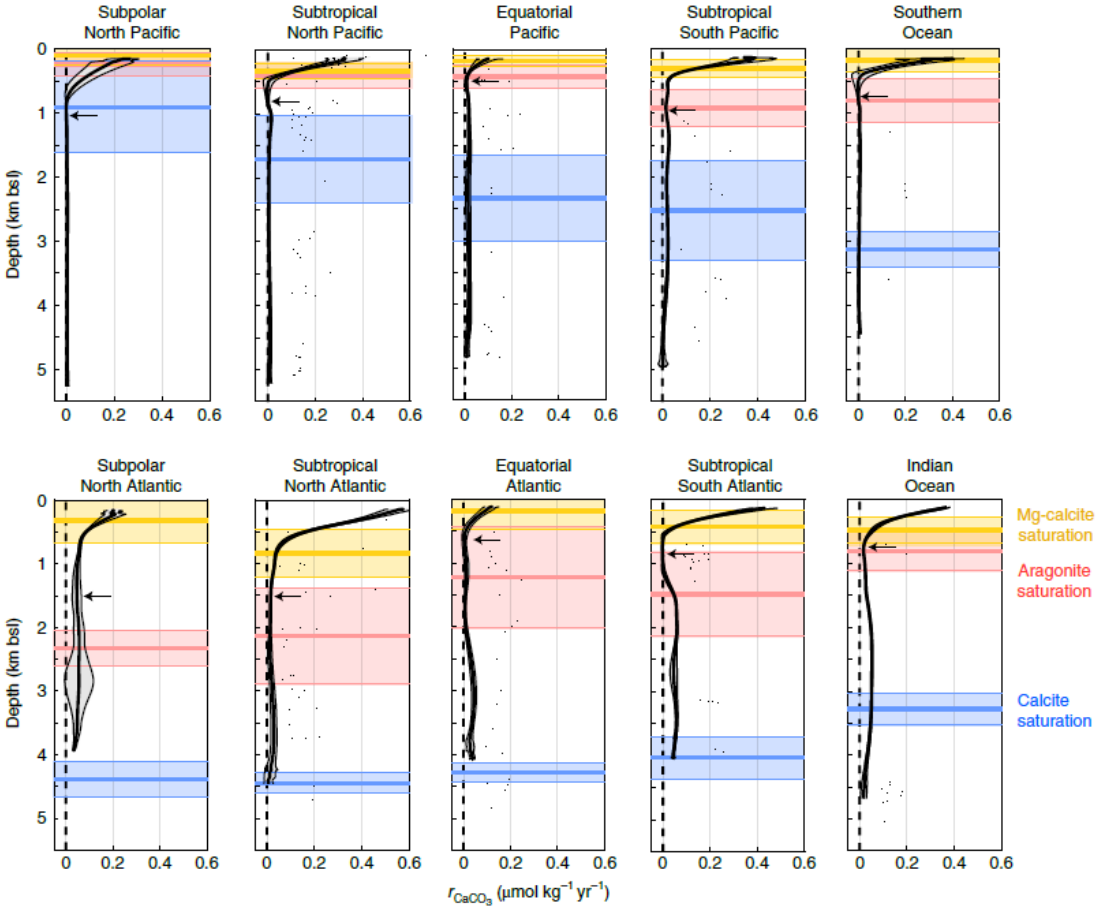

Fig 2. Regional profiles of reconstructed CaCO3 dissolution rates and saturation horizons. In each panel, the central black line is the reconstructed regional mean total CaCO3 dissolution rate, and the grey envelope represents the 90% confidence interval, accounting for the regional variability and uncertainties associated with the seawater chemistry and age estimates. The regional mean Mg-calcite (yellow), aragonite (red) and calcite (blue) saturation depths are represented with their uncertainty envelopes (1σ). Black arrows mark the depth limit between the upper dissolution regime, driven by CO2 produced during microbial and/or animal respiration and by the presence of highly soluble Mg calcites, and the lower dissolution regime, driven by increased CaCO3 solubility in bulk solution at high pressure. This depth limit is computed as the shallowest depth at which the depth derivative of the vertical dissolution rate profile is equal to zero. bsl, below sea level.

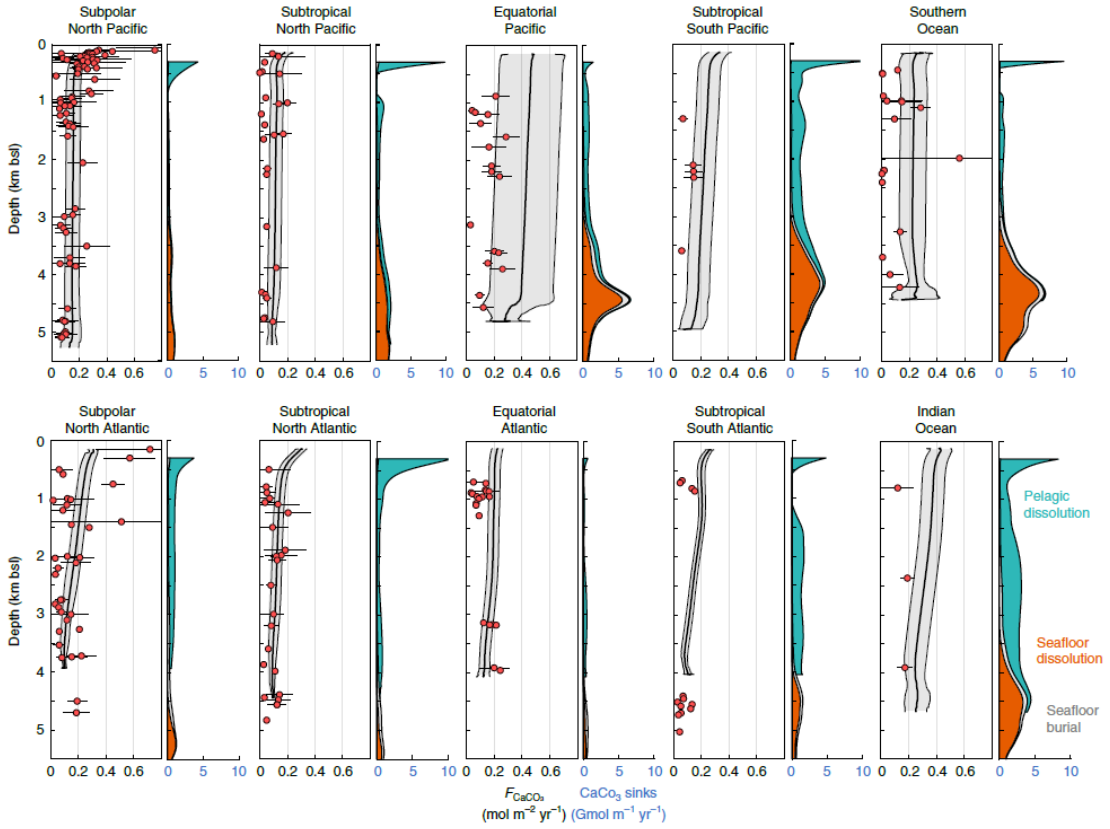

Fig 3. Reconstructed regional CaCO3 settling fluxes and depth distributions of their sinks. For each oceanic region, the central black line in the left panel is the reconstructed regional mean F_{CaCO3} (mol m^{-2} yr^{-1}), the grey envelope represents the 90% confidence interval, accounting for the regional variability and uncertainties associated with the seawater chemistry and age estimates. Red dots are $CaCO_3$ settling fluxes measured by sediment traps. Horizontal error bars associated with sediment-trap measurements represent the spatial and temporal variability of measurements originating from the same region and depth (1σ). For each region, the right panel shows the horizontally integrated $CaCO_3$ dissolution in the water column in turquoise, dissolution at the sediment–water interface in orange and burial in the sediments in grey ($CaCO_3$ sinks, Gmol m^{-1} yr^{-1}).

4. 加拿大东部大陆边缘物源及演化：来自中生代 Scotian 盆地铅同位素特征

翻译人：周洋 zhouy3@sustech.edu.cn

Aoife B, Georgia P P, David J W, et al. ***First-cycle sand supply and the evolution of the eastern Canadian continental margin: Insights from Pb isotopes in the Mesozoic Scotian Basins [J].*** *Geological Society of America Bulletin, 2021, 133, 1301–1319.*

https://doi.org/10.1130/B35707.1

摘要：物源分析对于理解、连接和重建源-汇系统和地表过程至关重要。加拿大东部沿海 Scotian 盆地的沉积物运移方向对于了解加拿大边缘 Labrador 裂谷演变至关重要，但是受到了沉积再循环的影响。在这项研究中，对整个 Scotian 盆地的 13 口钻井中碎屑钾长石 Pb 同位素进行了分析，以示踪物源。与以前的方法（锆石等重矿物）不同，碎屑钾长石不太可能在多个沉积循环中保存下来。铅同位素数据揭示了内陆物源在侏罗-白垩纪边界的动态跷跷板变化，反映了沿 Labrador 裂谷北向传播的隆升与下流域盆地断层系统重新激活之间复杂的相互作用。钾长石中的铅同位素记录表明，早在中部盆地 Callovian 期，从东部 Labrador 远距离供应逐渐增加，同时邻近阿巴拉契亚山脉的物源却在减少，但持续存在。与锆石等矿物进行比较，似乎会确定下流域盆地的沉积再循环，并突出显示了单独使用单个矿物（如锆石）的局限性。此研究可作为多种物源手段综合判别来源的一个实例，不仅可以解译古水流的方向，而且可以更好地将地球表面过程和构造事件的驱动力，机制以及时空范围联系在一起。

ABSTRACT: Provenance analysis provides a powerful means to understand, connect, and reconstruct source-to-sink systems and Earth surface processes, if reliable toolkits can be developed, refined, and applied. Deciphering sediment routing to the Scotian Basin, offshore eastern Canada, is marred by sedimentary recycling but is critical to understanding the evolution of the Canadian margin in response to the evolving Labrador rift. In this study, Pb isotopes in detrital K-feldspars were fingerprinted in 13

wells across the Scotian Basin to track first-cycle sand supply. Unlike previous approaches, which utilized less labile proxies such as zircon, detrital K-feldspars are unlikely to survive multiple sedimentary cycles. The Pb-isotopic data reveal a dynamic seesaw effect between hinterland sources across the Jurassic-Cretaceous boundary, reflecting the complex interplay between the northward propagation of uplift along the rising Labrador rift flank and the reactivation of fault systems in the lower drainage basin. Pb isotopes in K-feldspar record progressively increasing long-distance supply from eastern Labrador, as early as the Callovian in the central basin, alongside diminishing but persistent local sourcing from adjacent Appalachian terranes. Comparison with more resilient mineral proxies, notably zircon, appears to confirm recycling in the lower drainage basin and highlights the limitations of using a single mineral proxy in isolation. This case study serves as an example of the growing potential of multiproxy provenance toolkits not only to decipher sediment-routing corridors in paleodrainage systems, but to better define and connect the drivers, mechanisms, and spatial and temporal ranges of Earth surface processes and tectonic events.

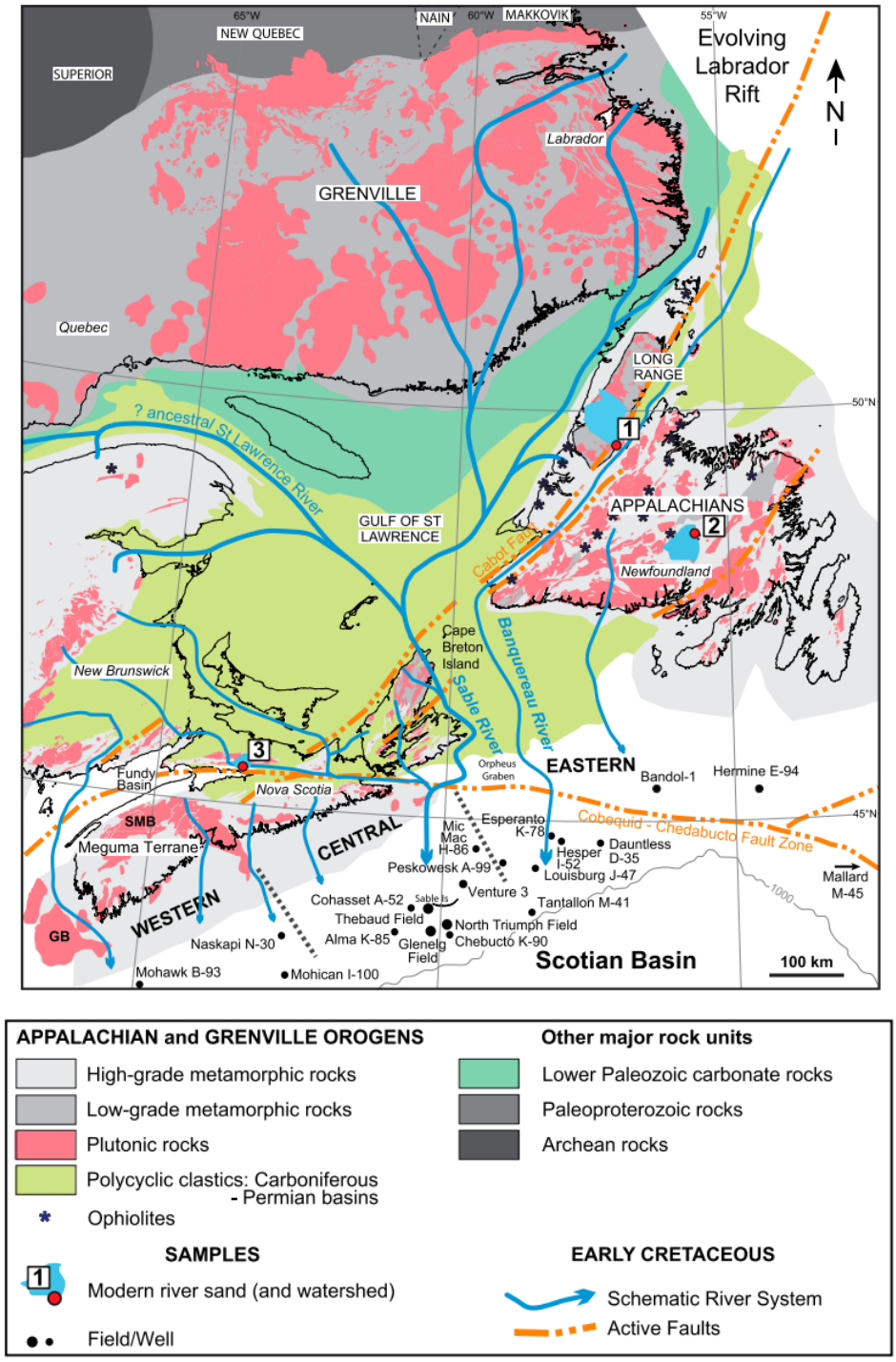

Fig1. Map of southeastern Canada showing distribution of plutonic rocks and locations of studied wells and modern river samples. Cretaceous drainage pathways inferred from previous detrital mineralogy studies are shown in blue. Dashed black lines define western, central, and eastern sectors of the Scotian Basin for the purposes of this study. GB—German Bank pluton, SMB—South Mountain Batholith. Figure is modified after Zhang et al. (2014).

5. Bransfield 伸展盆地第四纪火山群磁组构：Penguin Bridgeman 岛内部结构

翻译人：张琪 zhangq7@sustech.edu.cn

Oliva-Urcia B, López-Martínez J, Maestro A, et al., ***Magnetic fabric from Quaternary volcanic edifices in the extensional Bransfield Basin: internal structure of Penguin and Bridgeman islands (South Shetlands archipelago, Antarctica) [J]****. Geophysical Journal International, 2021, ggab177.*

https://doi.org/10.1093/gji/ggab177

摘要：研究火山群中的磁组构，特别是近期喷发的熔岩流，使我们能够了解与流动方向有关的矿物的定向分布，并对较老的和/或侵蚀的熔岩流进行恰当的描述。在这项工作中，介绍了最近（第四纪）熔岩流（七个轻微倾斜采样点和两个高原熔岩采样点）、火成岩沉积物（两个火成岩锥采样点）和位于 Bransfield 弧后盆地的 Penguin 岛和 Bridgeman 岛的火山锥、容颜穹顶和火山栓（三个采样点）的磁结构。这两个岛屿的火山活动与南 Shetlands 和南极半岛之间的 Bransfield 海峡的开裂而发生的断裂作用相关。岩浆物质的流动方向尚不清楚。岩石磁学分析、低温测量和电子显微镜观察（背散射电子成像和能量色散 X 射线分析）显示，贫钛磁铁矿（和磁赤铁矿）是磁组构的主要载体。赤铁矿可能存在于一些样品中。来自熔岩中心的样品显示了与流动平面平行或交织的磁线理，而在高原熔岩中，磁线理被包含在亚水平面内，除非在富含泡囊的样品中，磁线理发生交织。磁线理表明相对于扩张的 Bransfield 盆地轴线，Bridgeman 岛的流动方向是多变的。Penguin 岛的高原熔岩的流动方向是根据含有较多泡囊的叠瓦构造磁组构推断而来的，表明是东南-西北流动防线。火山穹顶也有向上流动的烙印，火山弹显示出分散的分布情况。

ABSTRACT: Studying the magnetic fabric in volcanic edifices, particularly lava flows from recent eruptions, allows us to understand the orientation distribution of the minerals related to the flow direction and properly characterize older and/or eroded flows. In this work, the magnetic fabric from recent (Quaternary) lava flows (slightly

inclined in seven sites and plateau lavas in two sites), pyroclastic deposits (two sites from a scoria cone) and volcanic cones, domes and plugs (three sites) from Penguin and Bridgeman islands, located in the Bransfield back-arc basin, are presented. The volcanism in the two islands is related to rifting occurring due to the opening of the Bransfield Strait, between the South Shetlands archipelago and the Antarctic Peninsula. The direction of flow of magmatic material is unknown. Rock magnetic analyses, low temperature measurements and electron microscope observations (back-scattered electron imaging and Energy Dispersive X-ray analyses) reveal a Ti-poor magnetite (and maghemite) as the main carrier of the magnetic fabric. Hematite may be present in some samples. Samples from the center of the lavas reveal a magnetic lineation either parallel or imbricated with respect to the flow plane, whereas in the plateau lavas the magnetic lineation is contained within the subhorizontal plane except in vesicle-rich samples, where imbrication occurs. The magnetic lineation indicates a varied flow direction in Bridgeman Island with respect to the spreading Bransfield Basin axis. The flow direction in the plateau lavas on Penguin Island is deduced from the imbrication of the magnetic fabric in the more vesicular parts, suggesting a SE-NW flow. The volcanic domes are also imbricated with respect to an upward flow, and the bombs show scattered distribution.

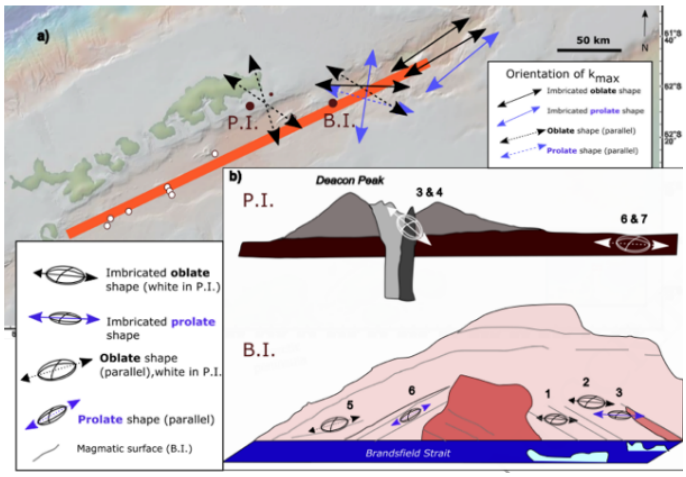

Fig1. Schematic representation of the magnetic lineation in a) map view of the lavas, and b) in cross-section (not to scale) on Penguin (P.I.) and Bridgeman (B.I.) islands of selected sites. On Penguin Island the volcanic plug ellipsoid is also added (center of the island). Continuous (discontinuous) line with arrow: magnetic lineation in imbricated (parallel to lava surface) ellipsoids. Black: oblate shape, purple: prolate shape. Orange line in a): simplification of the orientation of the spreading axis in the Bransfield Basin.

6. 混动无人机便携式机载磁测系统的磁干扰实验

翻译人：曹伟 11930854@qq.com

Krishna V, Lima Simões da Silva E, Døssing A. ***Experiments on magnetic interference for a portable airborne magnetometry system using a hybrid unmanned aerial vehicle (UAV)[J].*** *Geoscientific Instrumentation, Methods and Data Systems, 2021, 10(1): 25-34.*

https://doi.org/10.5194/gi-10-25-2021

摘要：使用无人机（UAV）进行航空磁测，不仅可以改善效果和快速采样，还可以降低作业成本。更重要的是，无人机载航空磁测可以进行低空测量，这使得测量结果可以像地面磁测效果一样精细明显。由于机载电子器件的强磁干扰，研制无人机航磁测量系统具有很大的挑战性。本文对某型号垂直起降混动型无人机进行了静磁干扰试验，并对其干扰程度进行了评估。静态实验结果表明，由于靠近伺服电机和发动机，机翼区域具有很强的磁性，而沿无人机纵轴的区域具有相对较小的磁性特征。在静态实验和空气动力学模拟的辅助下，我们首先提出了带有两个紧凑型磁力计的前置安装解决方案。随后，使用该设置进行了两个动态实验，以评估系统的动态干扰。动态实验的结果表明，飞行中电磁干扰的最强来源是将电池连接至飞行控制器的载流电缆，并且这种影响在飞机的俯仰操纵过程中影响最大。

ABSTRACT: Using unmanned aerial vehicles (UAVs) for airborne magnetometry offers not only improved access and rapid sampling but also reduced logistics costs. More importantly, the UAV-borne aeromagnetometry can be performed at low altitudes, which makes it possible to resolve fine features otherwise only evident in ground surveys. Developing such a UAV-borne aeromagnetometry system is challenging owing to strong magnetic interference introduced by onboard electric and electronic components. An experiment concerning the static magnetic interference of the UAV was conducted to assess the severity of the interference of a hybrid vertical take-off and landing (VTOL) UAV. The results of the static experiment show that the wing area is

highly magnetic due to the proximity to servomotors and motors, whereas the area along the longitudinal axis of the UAV has a relatively smaller magnetic signature. Assisted by the static experiment and aerodynamic simulations, we first proposed a front-mounting solution with two compact magnetometers. Subsequently, two dynamic experiments were conducted with the setup to assess the dynamic interference of the system. The results of the dynamic experiments reveal that the strongest source of in-flight magnetic interference is the current-carrying cables connecting the battery to the flight controller and that this effect is most influential during pitch maneuvers of the aircraft.

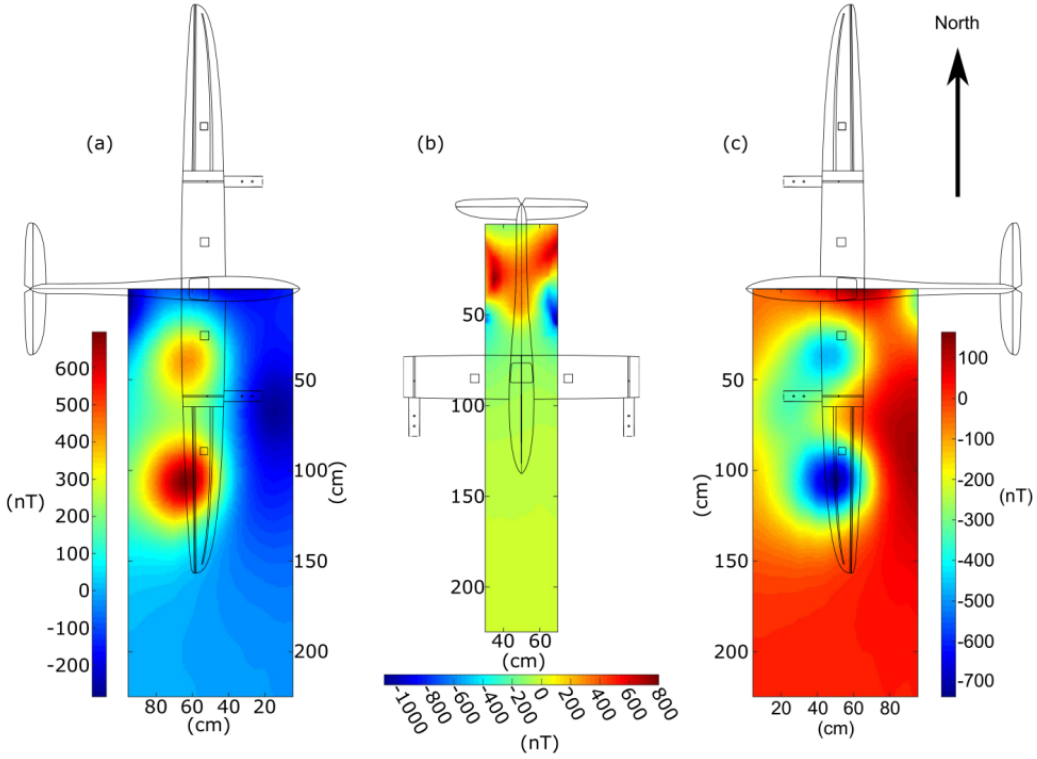

Fig 1. The diurnal-corrected and background-subtracted magnetic signature: (a) the starboard wing, (b) the area along the longitudinal axis of the UAV, and (c) the port wing.

7. 东赤道太平洋加拉帕戈初级生产力的控制因素（150-110ka）

翻译人：王敦繁 dunfan_w@foxmail.com

Collazos, L, Calvo, E, Schouten, S, et al. ***Controls on Primary Productivity in the Eastern Equatorial Pacific, East of the Galapagos Islands, During the Penultimate Deglaciation[J].*** *Paleoceanography and Paleoclimatology, 2020, 35(7).*

https://doi.org/10.1029/2019PA003777

摘要：赤道东太平洋（EEP）地区现代生物地球化学条件的特点是高营养盐低叶绿素。由于初级生产者对全球碳循环有重大影响，该地区的古生产力与气候变化和养分供应的关系一直是许多研究的主题。然而，这一地区特别是加拉帕戈斯群岛以东地区的复杂动力学因素，在将重建的古生产力与更高初级生产力的潜在机制联系起来时往往导致一些差异。这里我们重建了单体藻类和硅藻的初级生产力，以及大陆物质输入、海面盐度和海面温度，并将这些与 150-110ka（倒数第二次冰消期）时期现有的记录进行比较。我们的结果表明，倒数第二次冰消期间，EEP 区域的上升流增强，浮游植物丰度增加，这主要是由于赤道潜流对富含营养物质的南大洋来源水域的影响增加，以及大气沉降对铁的输入增加。倒数第二次冰消期间，由于全球大气和海洋重组和北大西洋 Heinrich Event 11 导致了营养物质的最大输入及浮游植物丰度增加。

ABSTRACT: Modern biogeochemical conditions of the Eastern Equatorial Pacific (EEP) region are characterized by high macronutrient concentrations but low phytoplankton abundance due to both iron and silicic acid limitation. Since primary producers significantly impact the global carbon cycle, paleoproductivity in relation to climate change and nutrient availability in this region has been a topic of a number of studies. However, the complex dynamics of this region, especially east of the Galapagos Islands, has led to some discrepancies when linking reconstructed paleoproductivity with potential mechanisms for higher primary productivity. Here we focus on reconstructing primary productivity of haptophyte algae and diatoms, as well as

continental material input, sea surface salinity, and sea surface temperature, and compare these reconstructions with existing records for the period comprised between 150 and 110 ka (the penultimate deglaciation period) with the aim to understand the mechanisms that most significantly influence phytoplankton growth over the EEP region east of the Galapagos Islands. Our results suggest enhanced upwelling in the EEP system during the penultimate deglaciation and increased phytoplankton abundance mainly as the result of both the increasing influence of nutrient-rich Southern Ocean sourced waters through the Equatorial Undercurrent and a higher input of iron through atmospheric deposition. The highest phytoplankton abundances recorded at the study site during the penultimate deglaciation also suggest that maximum input of nutrients might have occurred during the millennial-scale event Heinrich Event 11 in the North Atlantic as a result of global atmospheric and oceanic reorganizations.

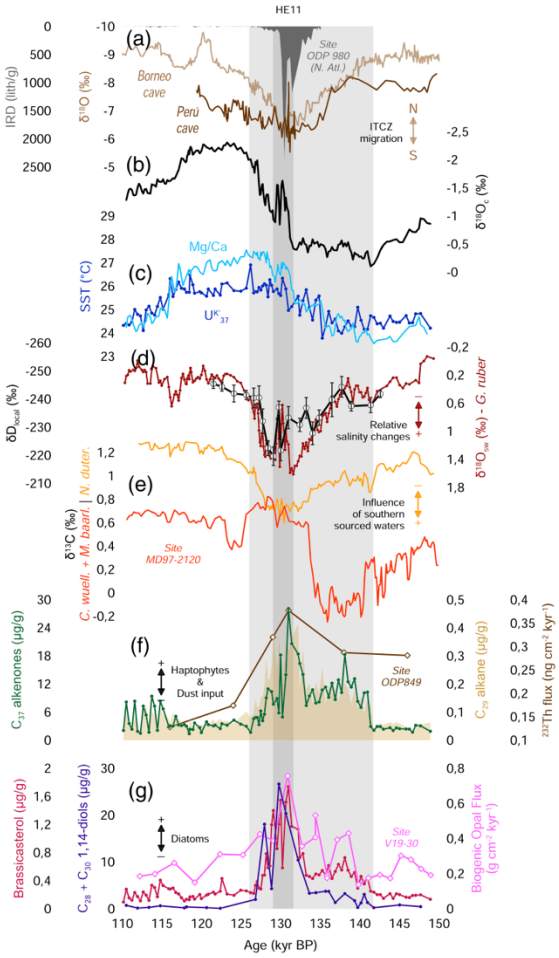

Fig1. Multiproxy records from ODP Site 1240 spanning the period between 150 and 110 ka and their comparison with other available climate records.

8. 西非 Barberton 绿岩带 3.5-4.0Ga 锆石的古地磁研究

翻译人：张伟杰 12031188@mail.sustech.edu.cn

Fu RR, Drabon N, Wiedenbeck M, et al. ***Paleomagnetism of 3.5-4.0Ga zircons from the Barberton Greenstone Belt, South Africa [J].*** *Earth and Planetary Science Letters. 2021,567:116999. https://doi.org/10.1016/j.epsl.2021.116999*

摘要：在地球历史的最初十亿年间，地核发电机的存在与否跟地球内部的热状态和早期大气层的组成密切相关。由于缺乏保存完好的超过 35 亿年的岩石单元，因此推动了利用碎屑锆石进行古地磁研究。然而，对来自澳大利亚 Jack Hills 的锆石研究发现，次生铁磁性矿物的普遍存在使人们对这些锆石记录>3.5Ga 地磁场的能力产生了怀疑。本文报道了来自南非 Barberton 绿岩带(BGB)的 19 个锆石的古地磁分析结果，这些锆石的结晶年龄为 3.5 ~ 4.0 Ga，其变质程度低于所有已知的老于 3.5Ga 其他地区的碎屑锆石。我们发现，BGB 锆石的磁矩比 Jack Hills 锆石弱近一个数量级，无法保留原始的古地磁信息。这一结果证实了来自 Jack Hills 和其他太古宙锆石的发现：即可能是由于辐射损伤诱发的渗透率提高，导致在沉积搬运和变质过程中，原始的铁磁性包裹体很容易从锆石中消失。通过古地磁测定 3.5Ga 之前的地球发电机活动可能需要利用其他具有较低辐射损伤的碎屑颗粒或没有受到高度变质作用的全岩样品。

ABSTRACT: The existence of a core dynamo during the first billion years of Earth history is closely related to the thermal state of the Earth's interior and composition of the early atmosphere. The scarcity of well-preserved rock units older than 3.5 billion years (Ga) has motivated the paleomagnetic analysis of detrital zircons. Studies of zircons from Jack Hills, Australia, however, have found the pervasive occurrence of secondary ferromagnetic minerals, casting doubt on the ability of these zircons to record a >3.5Ga geomagnetic field. Here we report paleomagnetic analyses on a set of 19 zircons with crystallization age 3.5-4.0Ga from the Barberton Greenstone Belt (BGB)

of South Africa, which have undergone lower grade metamorphism compared to all other known >3.5Ga detrital zircon localities. We find that BGB zircons have magnetic moments nearly one order of magnitude weaker than Jack Hills zircons, precluding the retention of primary paleomagnetic information. This result corroborates findings from the Jack Hills and other Archean zircon populations that primary ferromagnetic inclusions are readily eliminated from zircons during sedimentary transport and metamorphism, likely facilitated by radiation damage-induced permeability. Paleomagnetic determination of geodynamo activity prior to 3.5Ga may require investigation of other detrital grains with lower radiation damage potential or whole-rock samples that have escaped high degree metamorphism.

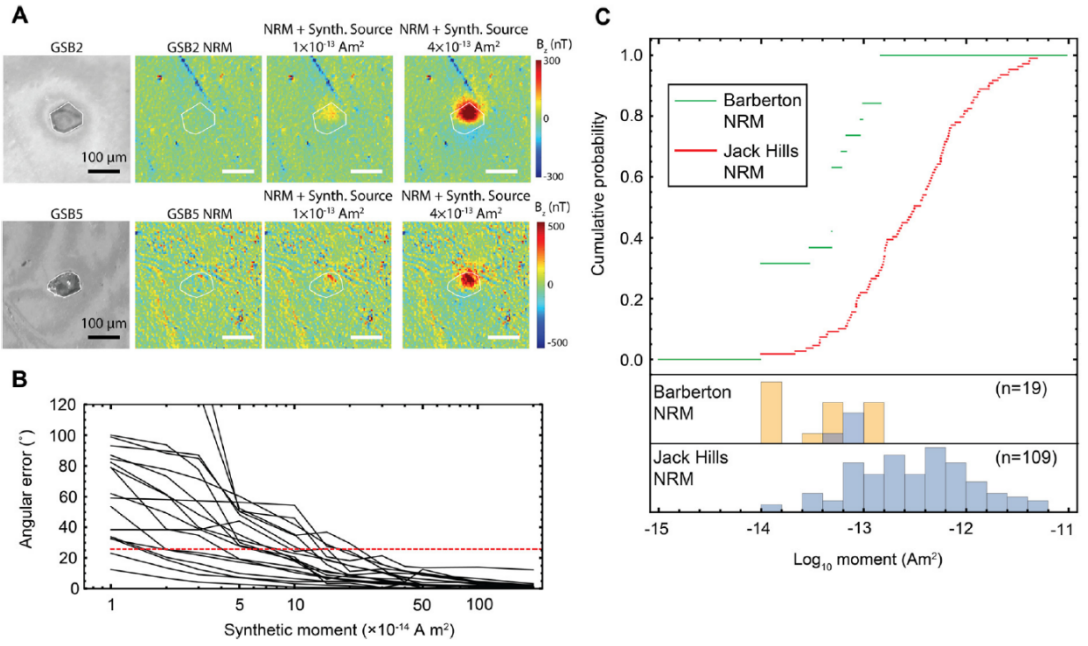

Fig1. Analysis of maximum permissible moment in signal-free zircons and statistical comparison of BGB and Jack Hills zircon NRMs. (A) QDM maps of vertical magnetic field with added synthetic source with the indicated moment. These maps are analyzed using a dipole inversion routine following Fu et al. (2020b) and the recovered moments are compared to that of the synthetic source. (B) Angular difference between recovered and synthetic source moments. Sources are classified as recovered if angular error falls below 25.8◦ (dashed red line) for two consecutive moments. This magnetic moment is then interpreted as the maximum permissible moment of the zircon. (C) Histograms of NRM magnetic moment (bottom) and cumulative probability distribution (top) of

BGB and Jack Hills zircons. Blue and yellow colors in the histograms indicate measured moments and computed upper bounds, respective.

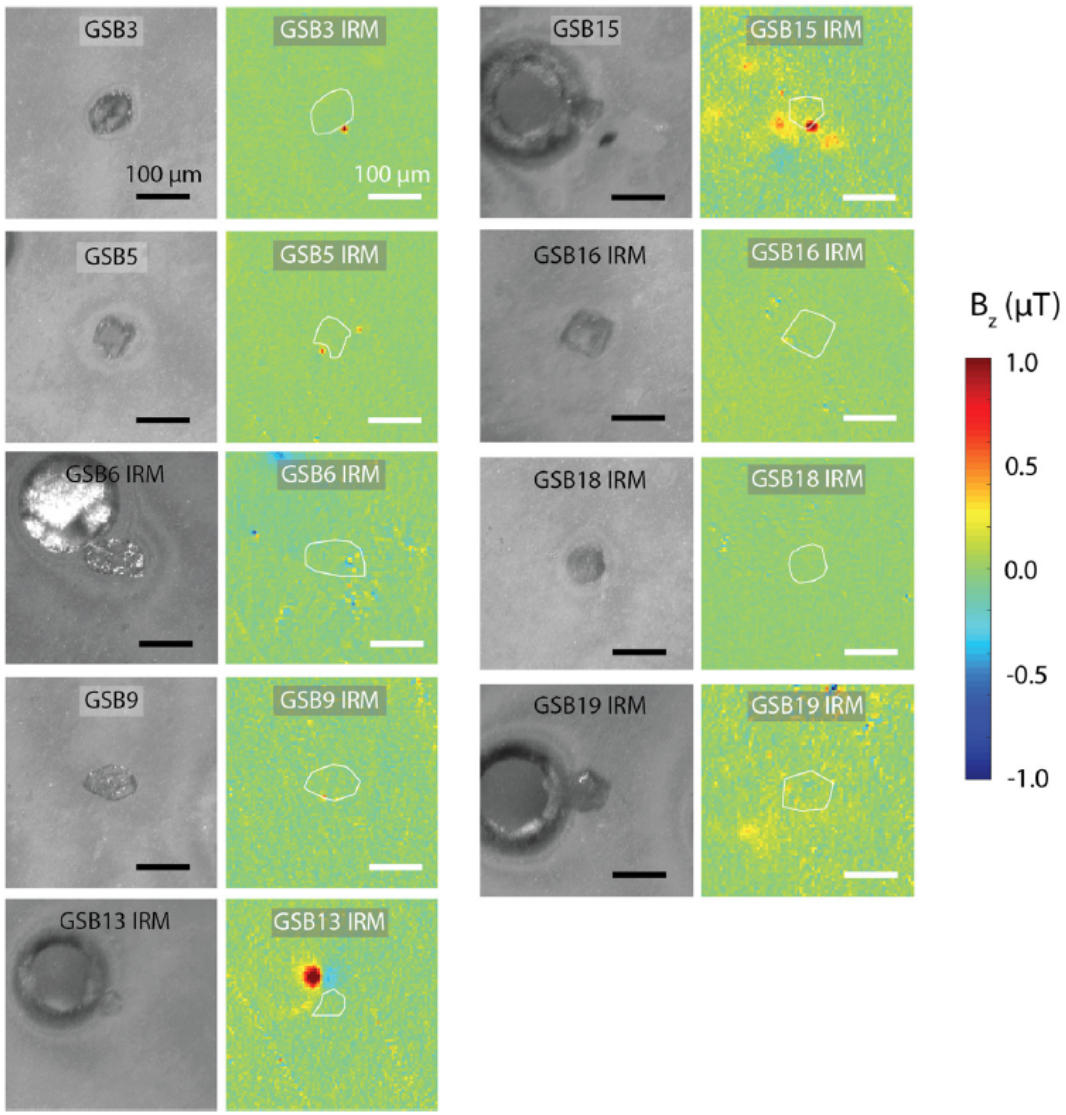

Fig2. QDM magnetic field maps of zircons pulsed with a 2T field in the out-of-plane direction. Positive magnetic field values correspond to fields out of the plane.

9. 新仙女木撞击假说:撞击证据综述

翻译人：李海 12031330@mail.sustech.edu.cn

Sweatman, M B, ***The Younger Dryas impact hypothesis: Review of the impact evidence[J].*** *Earth-Science Reviews, 2021, 103677.*

https://doi.org/10.1016/j.earscirev.2021.103677

摘要： Firestone 等人提出在 10835 cal BCE 左右发生了一次剧烈的撞击引发新仙女木气候事件，造成人类文化的变化和巨型动物的灭绝。这项工作开展 14 年以来，许多科研团队所进行的研究取得了压倒性的共识，表明他们所主张撞击假说应被接受，本文将对此进行综述。其主要的证据是在四大洲，尤其是北美和格陵兰发现的 YD（新仙女木）边界的地球化学记录，例如铂、淬火熔融材料和纳米金刚石。他们的其他主张尚未得到证实，但事件的规模，包括大范围的野火，其与 YD 事件的急剧降温时间相近，表明他们的假说是合理的，应进一步研究。值得注意的是，一部分研究人员反对撞击假说，但在细致的研究后，反对者所提供的证据可以解释为支持撞击假说。

ABSTRACT: Firestone et al., 2007, PNAS 104(41): 16,016–16,021, proposed that a major cosmic impact, circa 10,835 cal. BCE, triggered the Younger Dryas (YD) climate shift along with changes in human cultures and megafaunal extinctions. Fourteen years after this initial work the overwhelming consensus of research undertaken by many independent groups, reviewed here, suggests their claims of a major cosmic impact at this time should be accepted. Evidence is mainly in the form of geochemical signals at what is known as the YD boundary found across at least four continents, especially North America and Greenland, such as excess platinum, quench-melted materials, and nanodiamonds. Their other claims are not yet confirmed, but the scale of the event, including extensive wildfires, and its very close timing with the onset of dramatic YD cooling suggest they are plausible and should be researched further. Notably, arguments by a small cohort of researchers against their claims of a major impact are, in general,

poorly constructed, and under close scrutiny most of their evidence can actually be interpreted as supporting the impact hypothesis.

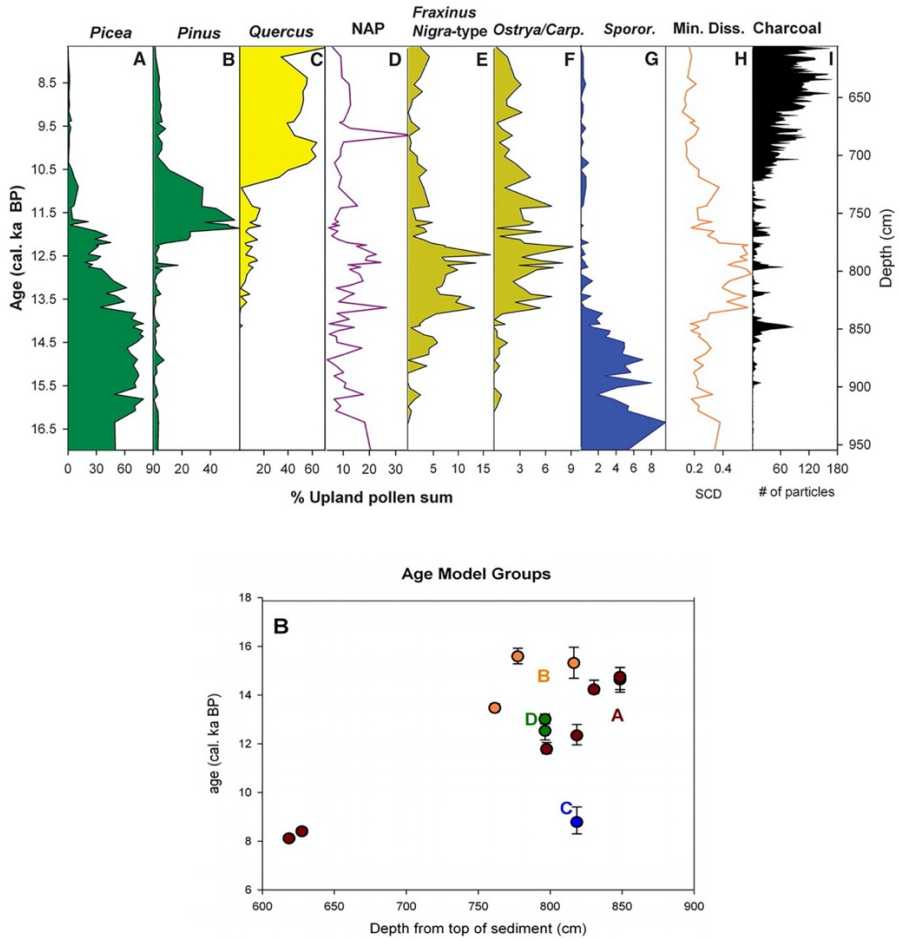

Fig1. a) Fig. 2 from Gill et al. (2009) showing the variation with sediment depth of a range of markers (upper plot). Note the prominent charcoal spike at 850 cm, which just precedes the onset of a dramatic change in pollen (signalled by the 'minimum dissimilarity', or Min. Diss.), and therefore climate lasting around 1500 years. This is likely the onset of the Younger Dryas period. b) Radiocarbon measurements from which Gill et al. (2009) constructed their age-depth model. Clearly, there is sufficient uncertainty in this data such that 850 cm might correspond to the onset of Younger Dryas cooling, circa 12,800 cal BP. Gill et al. (2009) construct their age-depth model by linear regression through the data points in groups A and D only, and they fail to report the uncertainty in the coefficients of their fitted line. Reproduced with permission from the AAAS.

10. 北冰洋冷却机在暖期的极向加强

翻译人：张亚南zhangyn3@mail.sustech.edu.cn

Qi Shu, Qiang Wang, Zhenya Song, et al, ***The poleward enhanced Arctic Ocean cooling machine in a warming climate[J].*** *Nature Comminications, 2021, 12, 2966.*

https://doi.org/10.1038/s41467-021-23321-7.

摘要：作为北冰洋的“冷却机”，Barents Sea 释放了大部分来自北大西洋的海洋热量。相关的海-气热交换在调节气候和决定北冰洋及其外部深海环流方面具有重要的作用。据报道，北冰洋的冷却效率在明显的下降。在本文研究中，作者发现北冰洋总体冷却效率并未下降：当 Barents Sea 南部冷却效率下降时，在更靠近极区的 Northern Barents Sea 和 Kara Sea 则会增加。这表明“冷却机”的向极扩张。根据气候模型预测，在气候变暖的情况下，“冷却机”会继续向 Kara Sea 扩张，然后到达 Arctic Basin。因此，北极的大西洋化将在未来加强并向极地推进。

ABSTRACT: As a cooling machine of the Arctic Ocean, the Barents Sea releases most of the incoming ocean heat originating from the North Atlantic. The related air-sea heat exchange plays a crucial role in both regulating the climate and determining the deep circulation in the Arctic Ocean and beyond. It was reported that the cooling efficiency of this cooling machine has decreased significantly. In this study, we find that the overall cooling efficiency did not really drop: When the cooling efficiency decreased in the southern Barents Sea, it increased in the northern Barents and Kara Seas, indicating that the cooling machine has expanded poleward. According to climate model projections, it is very likely that the cooling machine will continue to expand to the Kara Sea and then to the Arctic Basin in a warming climate. As a result, the Arctic Atlantification will be enhanced and pushed poleward in the future.

.

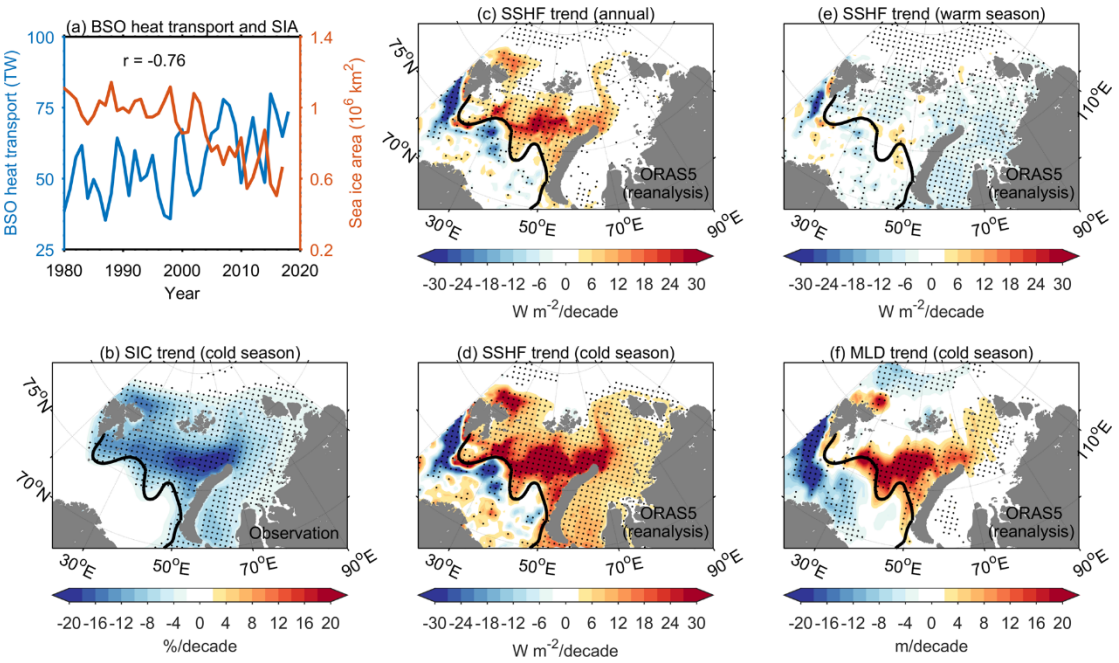

Fig 1. Climate change in the Barents and Kara Seas in the past. a. The time series of ocean heat transport through the Barents Sea Opening (BSO) and the cold season (October–March) sea ice area (SIA) in the Barents and Kara Seas. The linear trends of b cold season sea ice concentration (SIC), c. annual mean sea surface heat flux (SSHF), d. cold season sea surface heat flux, e. warm season (April–September) sea surface heat flux, and f cold season mixed layer depth (MLD) of 1979/80–2017/18. Dots indicate that linear trends exceed the 95% confidence level. The black lines in b–f are the 0 °C surface isotherm based on climatology from WOA13, which can represent the boundary between the southwestern and northern Barents Sea. Upward sea surface heat flux is positive. Ocean heat transport (a), SSHF (c, e, d), and MLD (f) are from the Ocean ReAnalysis System 5 (ORAS5). Satellite observed SIA (a) and SIC (b) are from the National Snow and Ice Data Center.

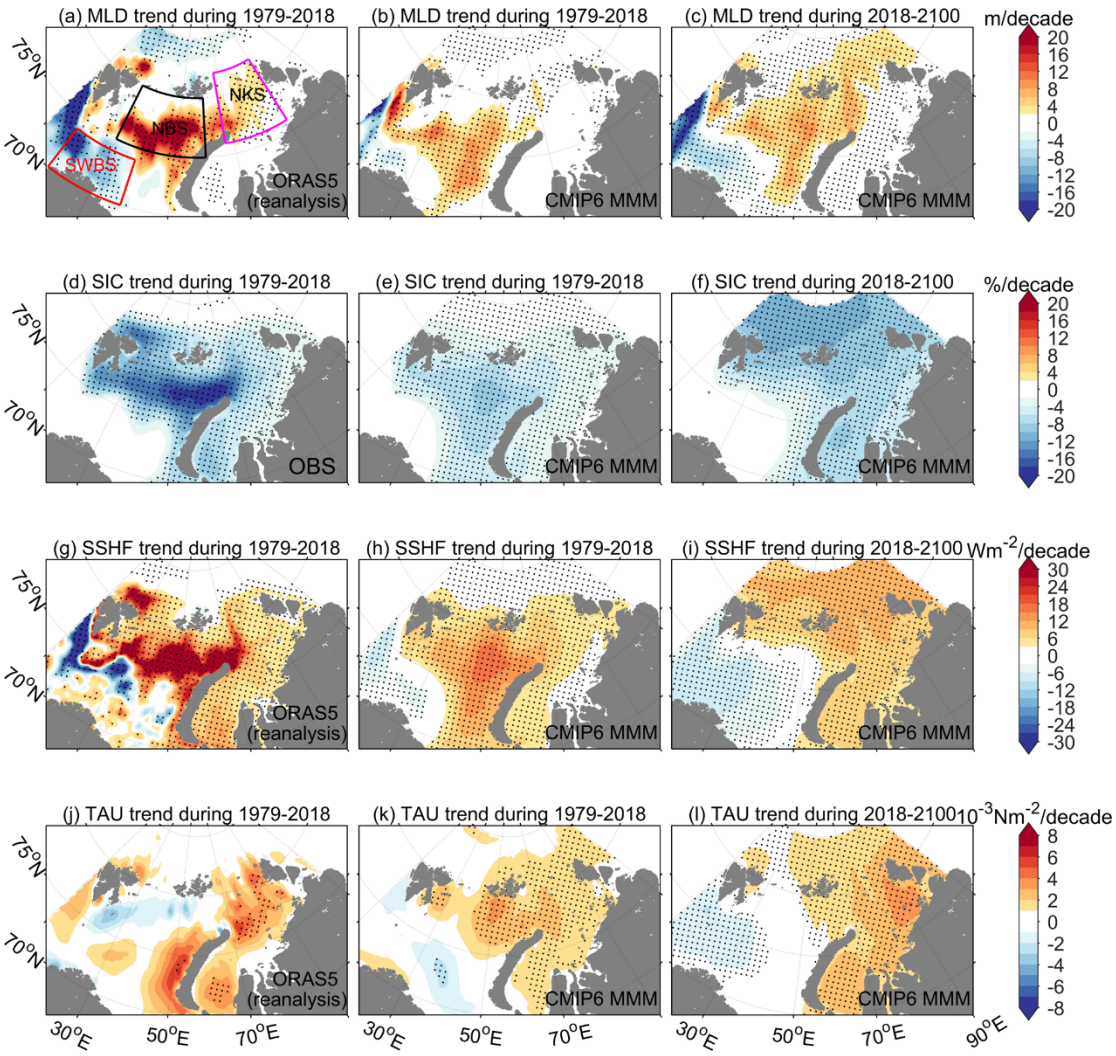

Fig2. Climate change in the CMIP6 models compared with observation and reanalysis. a–c: The linear trend of cold season mixed layer depth (MLD), d–f sea ice concentration (SIC), g–i sea surface heat flux (SSHF), and j–l sea surface wind stress (TAU) in the observation (OBS), reanalysis and CMIP6 multi-model mean (MMM). Dots indicate that linear trends exceed the 95% confidence level. Upward sea surface heat flux is positive. The red, black, and magenta boxes in a represent the southwestern Barents Sea (SWBS, that is, the Barents Sea Opening area), northern Barents Sea (NBS), and northern Kara Sea (NKS), respectively.

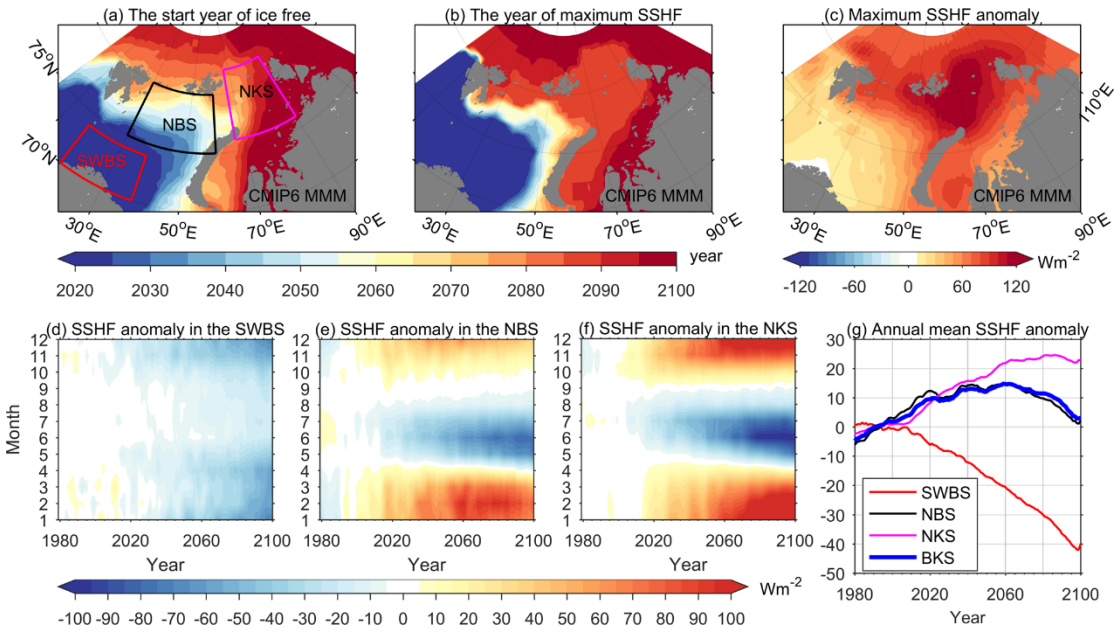

Fig3. The temporal and spatial evolution of the Arctic Ocean cooling machine. a The start year of being ice-free in the cold season during 2018/19–2099/2100. b The year of maximum cold-season sea surface heat flux (SSHF) anomalies during 2018/19–2099/2100. c The maximum of cold-season sea surface heat flux anomalies during 2018/19–2099/2100 referenced to the climatology. d–f Thirteen-year smoothed monthly sea surface heat flux anomalies averaged in the southwestern Barents Sea (SWBS), northern Barents and Kara Seas (NBS and NKS). g Thirteen-year smoothed annual mean sea surface heat flux anomalies averaged in the SWBS, NBS, NKS, and the entire Barents and Kara Seas (BKS). Anomalies are referenced to the mean over the period 1979–2008. The red, black, and magenta boxes in a indicate the areas used in d, e, and f, respectively.

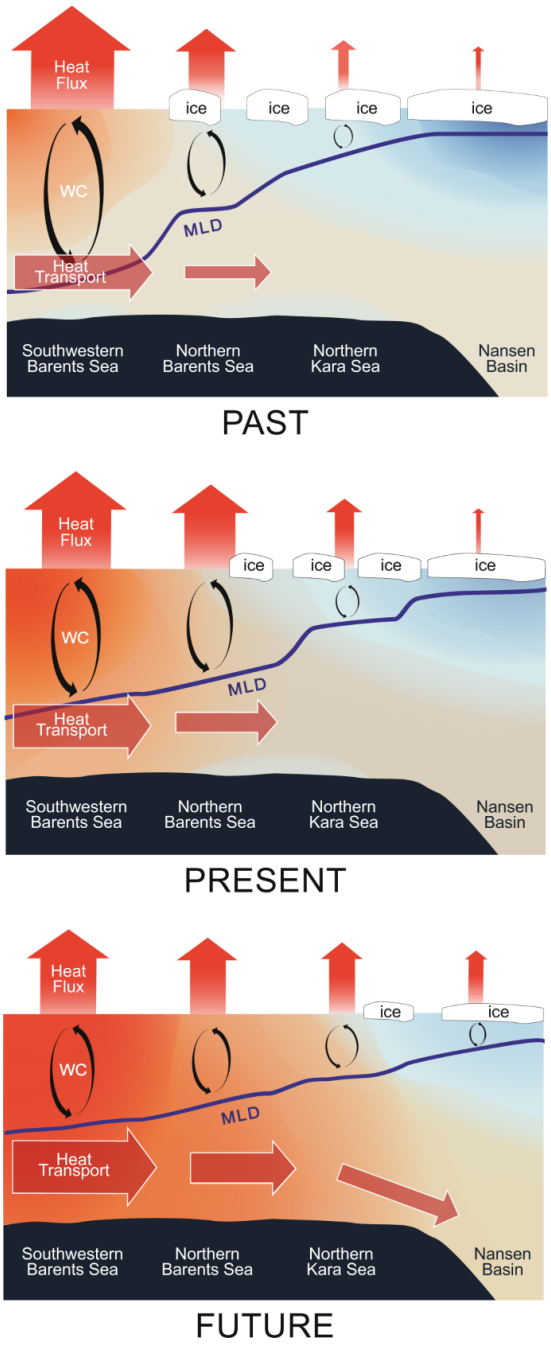

Fig 4. Poleward enhanced cooling machine and Arctic Atlantification. Conceptual schematic showing the related processes: ocean heat transport from the upstream increases because of the warming of the Atlantic Water inflow, but ocean surface heat release in the ice-free regions decreases due to more rapid atmosphere warming. Consequently, the mixed layer depth associated with winter convection decreases in the ice-free regions, and more heat is left in the ocean, leading to enhanced ocean warming in the downstream region. The latter induces stronger sea ice decline, more intensive ocean surface heat loss, and deeper mixed layer depth in winter in the downstream region. WC and MLD stand for winter convection and mixed layer depth, respectively.